Research Square

Preprints are preliminary reports that have not undergone peer review.
They should not be considered conclusive, used to inform clinical practice,
or referenced by the media as validated information.

A Reproducible Microfluidic Platform Combined with Deep Learning Image Analysis Enables Quantitative Single-Cell Characterization of Keratinocyte Responses to Flow

Miguel Del Valle-Fuentes
B5tec Solutions S.L.
Angélica Corral
Universidad Carlos III de Madrid
Alberto Bernaldo De Quirós
B5tec Solutions S.L.
Óscar Crespo-Toca
B5tec Solutions S.L.
Laura Aguado-Cabanillas
B5tec Solutions S.L.
Leticia Valencia
Universidad Carlos III de Madrid
Diego Velasco
Universidad Carlos III de Madrid
Alberto E. Quintero
aequinte@ing.uc3m.es

B5tec Solutions S.L.
Veronica Pena-Leon
B5tec Solutions S.L.

Article

Keywords:

Posted Date: November 10th, 2026

DOI: https://doi.org/10.21203/rs.3.rs-10528300/v1

License: This work is licensed under a Creative Commons Attribution 4.0 International License.
Read Full License

Additional Declarations: No competing interests reported.

A Reproducible Microfluidic Platform Combined with Deep Learning Image Analysis Enables Quantitative Single-Cell Characterization of Keratinocyte Responses to Flow

Miguel Del Valle-Fuentes[1], Angélica Corral[2], Alberto Bernaldo De Quirós[1], Óscar Crespo-Toca[1], Laura Aguado-Cabanillas[1], Leticia Valencia[2,3], Diego Velasco[2,3], Alberto E. Quintero[1,4,*,+], and Veronica Pena-Leon[1,*,+]

[1]R&D Department, B5tec Solutions S.L., Avda. Juan Caramuel 1, 28918, Madrid, Spain
[2]Department of Bioengineering, Universidad Carlos III de Madrid, Avda. de la Universidad 30, 28911, Madrid, Spain
[3]Institute of Health Research Jiménez Díaz Foundation, 28040 Madrid, Spain
[4]Department of Thermal Engineering and Fluids, Universidad Carlos III de Madrid, Avda. de la Universidad 30, 28911, Madrid, Spain
[*]aequinte@ing.uc3m.es, alberto.quintero@b5tec.com, veronica.pena@b5tec.com
[+]these authors contributed equally to this work

ABSTRACT

Advanced in vitro models require physiologically relevant culture conditions together with objective and reproducible methods for quantitative cell analysis. Here, we present an integrated microfluidic tissue culture platform combining controlled recirculating flow with a Human-in-the-Loop (HITL) deep learning workflow for quantitative single-cell analysis of dense keratinocyte cultures. The platform comprises a custom 3D-printed microfluidic bioreactor with automated flow regulation and was experimentally validated for biocompatibility. Immortalized human keratinocytes (HaCaT) cultured under continuous flow ($50\,\mu\mathrm{L/min}$) were compared with static controls. Fluorescence microscopy images were analyzed using a computational pipeline based on Z-projections, spatial upsampling, and iterative HITL fine-tuning of the Cellpose (cyto3) model. The optimized workflow improved single-cell detection by more than 140% compared with pretrained generalist segmentation models, enabling robust quantification of cell number, morphology, viability, and fluorescence marker expression in highly confluent cultures. Flow significantly increased metabolic activity, proliferation, cell area and diameter, and keratin 5 expression while preserving cell morphology. Under differentiation conditions, flow further enhanced keratin 10 (an early differentiation marker) expression while maintaining cell viability. This integrated platform provides a scalable framework for objective evaluation of advanced in vitro microphysiological systems, supporting biomedical research, Organ-on-a-Chip technologies, and New Approach Methodologies (NAMs).

Introduction

Animal models have played a fundamental role in biomedical research, enabling significant advances in drug development, vaccine production, and gene therapies[1]. However, the limited translation of some preclinical findings into human physiology, together with ethical and economic considerations, has stimulated the development of alternative experimental strategies[2]. Within this framework, the principles of 3Rs[3,4] and the emergence of New Approach Methodologies (NAMs) have promoted the adoption of human-relevant in vitro, ex vivo, and computational models that aim to reduce the reliance on animal experimentation while improving biological relevance and reproducibility[5–7].

Among emerging NAMs, microfluidic technologies have enabled the development of advanced in vitro systems capable of reproducing key aspects of the cellular microenvironment, including controlled nutrient delivery, waste removal, oxygen gradients, and mechanical stimulation[8]. The integration of microfluidics with cell culture has led to Organ-on-a-Chip (OoC) platforms, which provide physiologically relevant microscale environments for studying tissue behavior, disease mechanisms, and drug responses[9–12]. A notable milestone in this field has been the initial steps for regulatory approval of a Liver-on-a-Chip device for drug safety evaluation, demonstrating the growing confidence in these technologies as tools that complement traditional preclinical models[13]. Although these models

demonstrate the versatility of OoC technologies, their adoption within routine preclinical workflows remains limited by factors including device complexity, experimental variability, and challenges in standardization.

Among the different organ-specific applications of OoC technology, the skin represents a particularly relevant target because of its barrier, immunological, and homeostatic functions. In vitro skin models are widely used to evaluate pharmaceuticals, cosmetics, and medical devices, ranging from conventional 2D cultures to more advanced reconstructed tissues[14,15]. However, many models still rely on static culture conditions that fail to reproduce the dynamic mechanical and transport signals present in vivo[16]. Developing systems capable of providing stable, controlled, and well-characterized flow therefore represents an important step towards improving the functionality and predictive capacity of OoC technologies.

At the same time, the increasing sophistication of these platforms has generated large volumes of microscopy data that require robust and scalable analytical approaches. The widespread adoption of high-content microscopy has generated a growing need for automated and reproducible quantitative analysis methods. Manual evaluation of dense cell cultures remains time-consuming and susceptible to observer bias, particularly when assessing proliferation, viability, and phenotypic markers in large image datasets[17,18]. Consequently, reliable single-cell quantification has become a critical requirement for extracting biologically meaningful information from advanced in vitro models.

In particular, neural network-based segmentation tools such as Cellpose have demonstrated robust performance in various cell types and imaging conditions, allowing accurate identification of individual cells even in dense monolayers[19]. However, pre-trained models may exhibit limited generalization when faced with variations in staining protocols, imaging settings, or cell morphology, highlighting the need for customized training strategies and validation workflows adapted to specific experimental setups[20,21]. For this reason, Human-In-The-Loop (HITL) and fine-tuning validation strategies are increasingly adopted to improve segmentation accuracy and ensure reliable quantification of biological parameters in high-content microscopy datasets[22,23].

Together, these observations indicate that the advancement of physiologically relevant in vitro systems requires not only precise control of the cellular microenvironment but also reproducible and objective methods for quantifying cellular responses. Although considerable progress has been achieved in microfluidic culture technologies and AI-based image analysis independently, the integration of both approaches into reproducible and accessible experimental workflows remains limited.

In this study, we present a reproducible microfluidic tissue culture platform combining automated recirculating flow control with an AI-assisted image analysis workflow for quantitative single-cell characterization of keratinocyte responses under dynamic culture conditions. The platform incorporates custom 3D-printed bioreactors validated for biocompatibility and enables controlled medium perfusion within a compact and scalable workflow. Using HaCaT keratinocytes, we evaluated the effects of flow on proliferation, viability, morphology, and differentiation relative to conventional static culture conditions. To support objective data extraction, a Human-in-the-Loop (HITL) deep learning workflow based on Cellpose was developed and specifically optimized for quantitative analysis of highly confluent keratinocyte cultures. Together, the proposed framework enables reproducible assessment of cellular responses to flow and provides a quantitative methodology for objective evaluation of advanced in vitro and microphysiological systems.

Results

HITL-optimized deep learning workflow for single-cell segmentation and multiparametric analysis of confluent keratinocyte cultures

Manual quantification of cells in confluent keratinocyte monolayers is labor-intensive and susceptible to observer bias, particularly when assessing viability or quantifying diffuse cytoplasmic markers such as keratin 5 (K5) and keratin 10 (K10). To enable objective and reproducible single-cell analysis, microscopy images from Live/Dead staining and immunofluorescence assays (K5/K10) were processed using a deep learning-based workflow for automated cell segmentation.

The Cellpose algorithm (cyto3 model) was optimized to segment the high-density, contact-inhibited morphologies characteristic of immortalized human keratinocyte (HaCaT) cultures. Because cells in dense monolayers often span varying focal depths, a Sum Slices Z-projection was first applied to integrate the optical signal across focal planes (Figure 1a).

Using this enhanced input, the computational pipeline (Figure 1b) integrated spatial upsampling to mathematically expand cellular contours, followed by a HITL active learning loop. This cumulative iterative fine-tuning, where newly corrected images were continuously added to a growing training pool to sequentially update the model, progressively

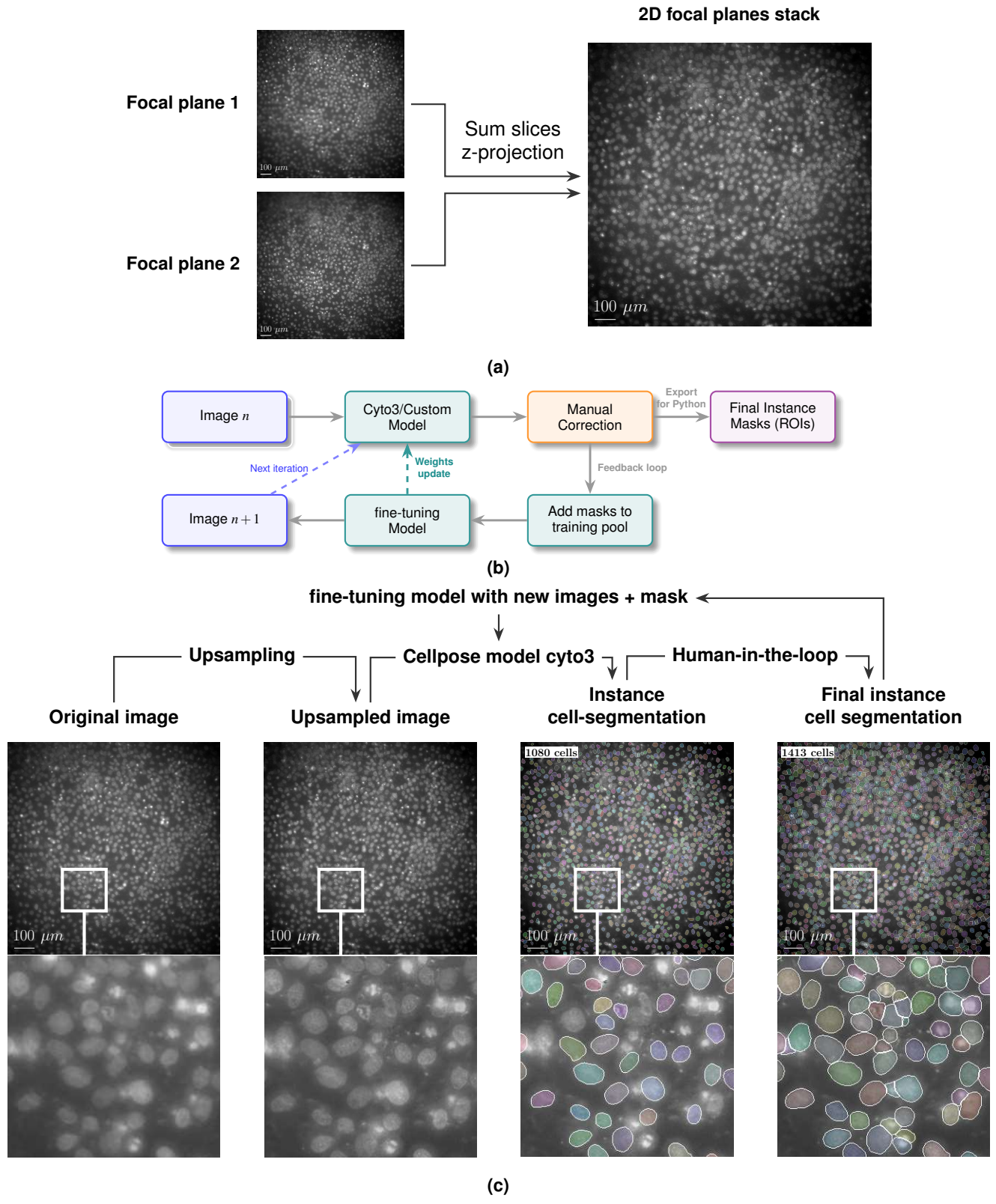


Figure 1. Single-cell segmentation workflow for the cyto3 fine-tuning HITL model. (a) Improved input image by multiple focal plane fusion by sum slices z-projection. (b) Fine-tuning HITL active learning architecture diagram for training cyto3 model to single-cell segmentation. (c) Original image, upsampled image, single-cell segmentation results in the pre-trained model and after fine-tuning with HITL.

reduced under-segmentation errors in regions of high cell density and variable fluorescence intensity. As shown in Figure 1c, this combined approach of spatial standardization and HITL training improved the ability of the model to delineate individual cellular boundaries compared to the baseline predictions.

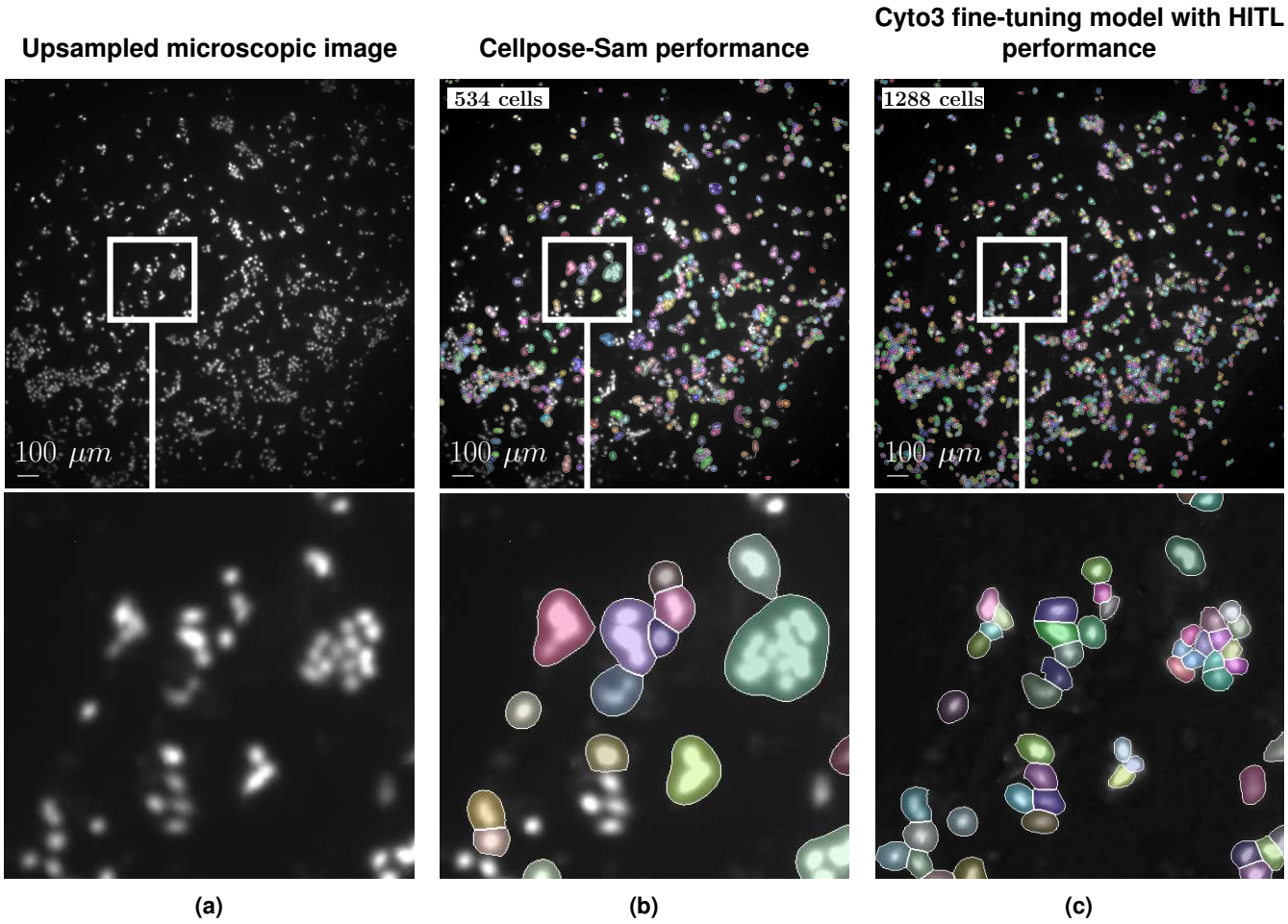


Figure 2. Models performance comparison for single-cell segmentation. (a) Upsampled input image. (b) Single-cell segmentation results obtained with Cellpose–Sam generalist algorithm. (c) Single-cell segmentation results obtained with cyto3 fine-tuning model with HITL active learning.

Figure 2 compares single-cell segmentation performance between the Cellpose–SAM generalist algorithm and the HITL fine-tuned cyto3 model in highly confluent keratinocyte cultures. The initial upsampled microscopic image used as input is shown in Figure 2a. As illustrated in the zoomed region of Figure 2b, the Cellpose–SAM generalist model frequently under-segments dense cellular regions, failing to identify individual cell boundaries and merging neighboring cells into one single object. This limitation resulted in a substantial underestimation of cell detection, with only 534 cells identified in the analyzed image. In contrast, the HITL-optimized cyto3 model, shown in Figure 2c, resolved adjacent cell boundaries within the same region, enabling precise single-cell segmentation, even under highly contact-inhibited growth conditions and heterogeneous fluorescence intensity. The HITL-optimized cyto3 model identified 1288 cells in the same image and resolved neighboring cell boundaries more effectively in dense regions.

These results show that iterative HITL fine-tuning markedly improved segmentation performance in confluent keratinocyte cultures, reducing under-segmentation and increasing the number of detected single-cell instances relative to a generalist segmentation model. Compared to the Cellpose-SAM generalist model, the HITL-optimized workflow increased single-cell detection by more than 140%, highlighting the importance of dataset-specific fine-tuning for quantitative analysis.

The workflow enabled objective, reproducible and scalable quantification of multiple descriptors at the single cell level, including cell number, size (area and equivalent diameter), morphology (eccentricity) and fluorescence

intensity for K5 and K10, as well as calcein-AM and ethidium homodimer-1 (Live/Dead staining), under both static and flow keratinocyte culture conditions, forming the basis for the analyzes presented in the following sections (Figures 3–6).

Platform design and material biocompatibility

A compact and automated flow control system was developed to emulate dynamic physiological conditions in vitro, providing controlled medium recirculation as part of the microfluidic tissue culture platform, mimicking aspects of the human circulatory system[24]. For more details, see Figure S1 and Figure S2. Recirculation capability enables operation with low medium volumes while supporting prolonged exposure of cells to endogenously secreted factors and dynamic culture conditions[25,26]. Its modular design enables the simultaneous operation of multiple independent units within a standard cell-culture incubator ensuring reproducibility, and its remote communication enables the system to operate without frequent incubator access during experiments.

Given the requirements for cell-culture applications, the materials used in the microfluidic platform were systematically evaluated for biocompatibility. Individual components were pre-incubated in culture medium for 72 hours, then HaCaT cells were seeded in commercial culture plates using the pre-incubated medium and cultured for 24 hours, as summarized in Figure S1b. Cytocompatibility was assessed using the alamarBlue™ assay. Standard culture medium and medium exposed to a cytotoxic reference material were used as positive and negative controls, respectively.

Figure 3a shows that all evaluated components exhibited significantly higher viability than the cytotoxic control. No significant differences were observed relative to the positive control, indicating that none of the tested materials induced detectable cytotoxic effects under the evaluated conditions.

In parallel, several commercially available 3D-printing resins were evaluated using the same procedure applied to the materials presented in Figure 3a, for the microfabrication of flow control system components and custom-designed bioreactors housing cell culture inserts. Biocompatibility was assessed using the alamarBlue™ assay, and all eight candidate resins exhibited significantly higher cell viability than the cytotoxic control (Figure 3b). Among the evaluated resins, Resin 3 was selected for the fabrication of 3D-printed components of the microfluidic tissue culture platform based on its favorable cytocompatibility profile and suitability for high-resolution fabrication.

To further validate these findings, Live/Dead assays were performed comparing a custom 3D-printed culture plate (made with Resin 3) with a standard commercial culture plate; optical fluorescence microscope images are shown in Figure 3c. These observations were consistent with the quantitative analysis obtained by the HITL fine-tuned cyto3 model of the previous section and shown in Figures 3d and 3e, where no significant differences in cell number or surface coverage were observed between custom 3D-printed culture plates and conventional commercial culture plates. Together, these results support the cytocompatibility of the selected resin and its suitability for subsequent microfluidic culture experiments. Following material validation, the selected resin and components were used for the fabrication of the bioreactor and flow control system used throughout subsequent flow culture experiments.

Optimization of keratinocyte seeding density

Following the validation of the cytocompatibility of the material, a cell-seeding optimization study was performed to determine an appropriate initial density for HaCaT culture within the microfluidic platform. Cells were seeded at three densities ($\mathrm{d1} = 100000$, $\mathrm{d2} = 150000$, and $\mathrm{d3} = 200000\ \mathrm{cells/cm^2}$) in both the custom 3D-printed bioreactor (Figure S2) and a conventional 24-well culture plate.

Cell growth was evaluated using the alamarBlue™ assay on days 1 and 3 (Figure 3f). To compare proliferative responses between conditions, results were expressed as the ratio between metabolic activity on day 3 and day 1 (Day 3/Day 1). All seeding densities exhibited increased metabolic activity over time, and similar trends were observed in both custom 3d-printed bioreactor and commercial culture plates. The lowest density $\mathrm{d1}$ produced the largest relative increase in metabolic activity, whereas higher initial densities as $\mathrm{d2}$ and $\mathrm{d3}$ showed smaller increments.

Based on these results, a seeding density of $100000\ \mathrm{cells/cm^2}$ was selected for all subsequent experiments, as it provided the largest dynamic range for detecting changes in cellular activity while maintaining comparable behavior between the custom 3d-printed bioreactor and conventional culture systems. This density was therefore used for subsequent culture experiments and quantitative single-cell analyses.

Flow promotes keratinocyte proliferation and increases cell area and diameter while preserving cell shape

Using the optimized seeding density ($\mathrm{d1} = 100000\ \mathrm{cells/cm^2}$), static and flow culture conditions were compared in the custom 3D-printed bioreactor. HaCaT cells were seeded in culture inserts and maintained under static conditions

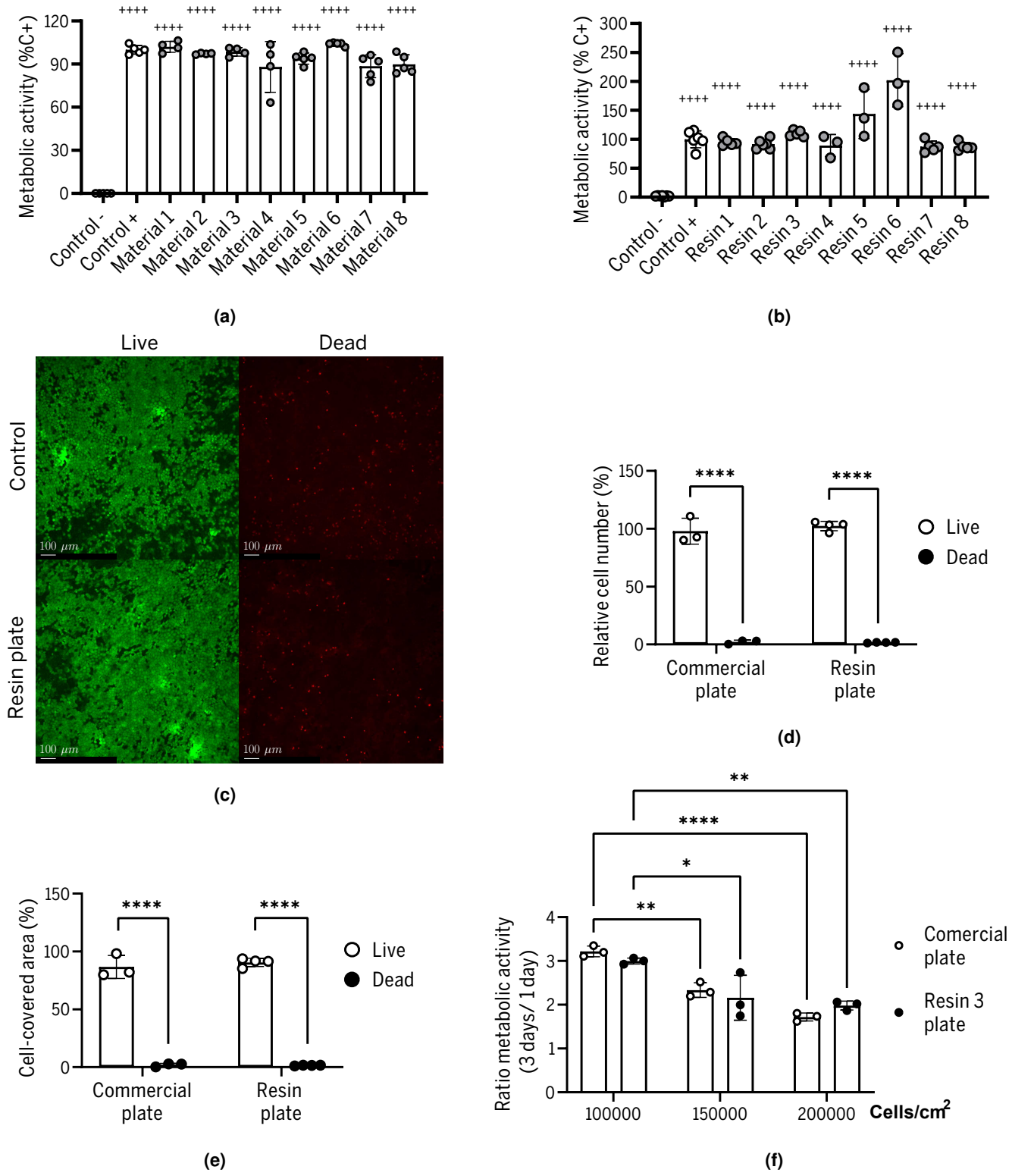


Figure 3. Evaluation of material biocompatibility and optimization of HaCaT cells seeding in a microfluidic bioreactor. (a)Biocompatibility of flow-system components assessed by alamarBlue™ with positive and cytotoxic controls. (b)Screening of 3D-printing resins for cytocompatibility. (c)Representative Live/Dead fluorescence images (20×) of HaCaT cells in "Resin 3" bioreactors and commercial plates. (d – e)Quantification of cell number and cell-covered area. (f)Seeding density optimization ($100\text{K} - 200\text{K cells/cm}^2$) over 3 days in custom 3D-printed bioreactors or commercial plates; metabolic activity expressed as Day 3/Day 1. Data are mean ± SD ($n = 3 - 5$). Statistical significance was determined by one– or two– way ANOVA with Dunnett's multiple comparisons tests ($^*p < 0.01$, $^{****}p < 0.0001$).

for 24 hours to allow cell attachment. Inserts were subsequently transferred to the bioreactors and cultured for an additional 24 hours either under static conditions or continuous flow ($50\ \mu\mathrm{L/min}$), as summarized in Figure S1c.

Flow culture was associated with higher metabolic activity than static culture, as determined by the alamarBlue™ assay (Figure 4a). Live/Dead staining showed higher viability under both conditions (Figure 4b). A cursory visual inspection of the fluorescence microscopy images suggests a higher live cell density under flow conditions compared with static culture. This qualitative observation was subsequently confirmed by quantitative image analysis using the HITL-optimized cyto3 model, which revealed a higher number of detected cells under flow conditions (Figure 4c), accompanied by increased cell-covered area (Figure 4d).

In addition to enhancing proliferation, continuous flow influenced keratinocyte morphology. Morphometric analysis of segmented cells, obtained from the single-cell segmentation workflow, revealed a significant increase in the mean projected cell area under flow conditions, increasing from approximately $525\ \mu\mathrm{m}^2$ in static conditions to $645\ \mu\mathrm{m}^2$ under flow, as can be seen in Figure 4e. Similarly, the mean cell diameter increased from around $25\ \mu\mathrm{m}$ in static cultures to $28\ \mu\mathrm{m}$ in flow cultured cells as shown in Figure 4f.

Nevertheless, the shape of the cells remained largely unchanged, as indicated by comparable eccentricity values between static and flow conditions in Figure 4g. These results suggest that flow not only promotes proliferation but also was associated with increased cell size while maintaining overall morphology. Importantly, these measurements were obtained through automated single-cell analysis of highly confluent cultures, enabling quantitative assessment of both population-level and morphological responses to flow.

To further investigate the effect of flow on the keratinocyte phenotype, immunofluorescence analysis was performed in HaCaT cells that were initially seeded in culture inserts and incubated for 24 hours under static condition, followed by 24 hours under static condition or under continuous flow ($50\ \mu\mathrm{L/min}$). Immunofluorescence staining was performed for K5, a basal proliferation marker, K10, an early differentiation marker, and Hoechst for nuclear labeling.

As shown in Figure 5a, the expression of K5 was higher under flow conditions compared to static conditions, consistent with an increase in the proliferative phenotype. This increase was observed in both the K5-positive area normalized to cell nuclei (Hoechst) with the calculated values presented in Figure 5b, and the K5 fluorescence intensity normalized to Hoechst presented in Figure 5c. Both metrics, obtained through the HITL-optimized single-cell analysis workflow, showed significant increases under flow conditions, consistent with the higher cell number and metabolic activity observed in the previous analyses. In contrast, K10 expression was undetectable in both static and flow conditions as can be seen in Figure 5a, consistent with cells remaining in a non-differentiated proliferative state under these conditions. Together, these results indicate that controlled flow enhances keratinocyte growth and K5 expression without detectable induction of K10 under proliferation conditions.

Flow enhances keratinocyte differentiation under differentiation conditions

HaCaT cells were seeded in culture inserts and maintained under static conditions for 24 hours in proliferation medium to allow cell attachment. Inserts were subsequently transferred to the bioreactors and cultured for an additional 72 hours under either static conditions or continuous flow ($50\ \mu\mathrm{L/min}$). During this period, proliferation medium was replaced with differentiation medium supplemented with ascorbic acid, a known inducer of keratinocyte differentiation, as summarized in Figure S1d.

Cell differentiation was assessed by immunofluorescence staining for K5, K10 and Hoechst for nuclear visualization, as shown in Figure 6a. Under these conditions, cells exposed to flow showed an increased expression of K5 compared to static culture, consistent with the proliferative response previously observed under proliferation conditions (Figure 5). This increase was reflected in both the K5-positive area and K5 fluorescence intensity normalized to cell number (Hoechst), as shown in Figures 6b and 6c, respectively.

Flow culture was also associated with increased K10 expression, as evidenced by significant increases in both K10-positive area and fluorescence intensity normalized to cell number (Hoechst) (Figures 6d and 6e). To account for differences in cell density between static and flow conditions, all marker quantifications were normalized to the number of nuclei identified through automated analysis of Hoechst-stained images using the HITL-optimized cyto3 workflow. This normalization indicates that the observed increases in K5 and K10 expression were not solely explained by differences in cell number.

Together, these results indicate that flow culture in differentiation medium was associated with increased expression of both K5 and K10, consistent with enhanced progression toward an early differentiated keratinocyte phenotype. Importantly, the automated single-cell analysis workflow enabled quantitative comparison of differentiation associated markers across culture conditions while minimizing observer-dependent bias.

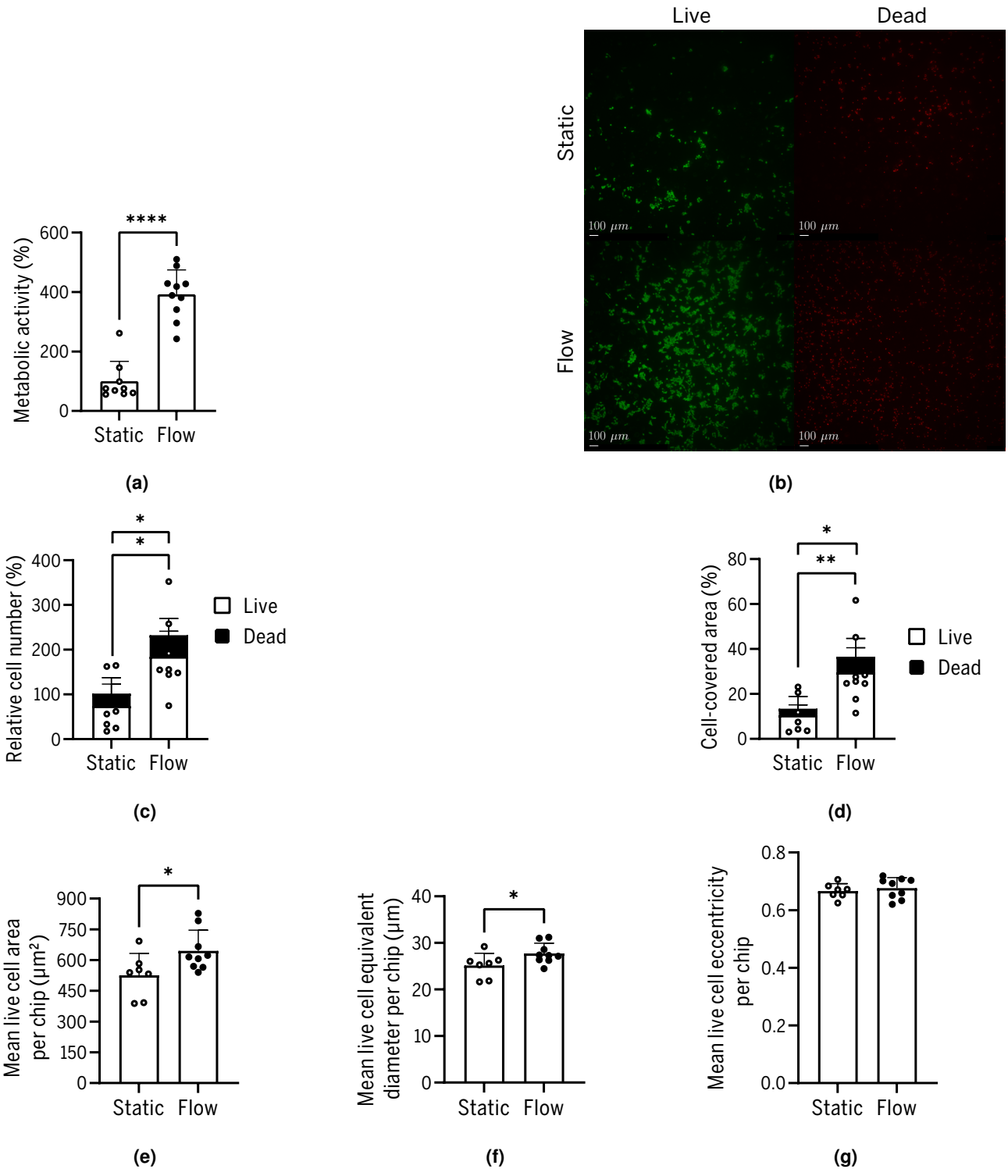


Figure 4. Dynamic perfusion enhances keratinocyte metabolic activity, viability, and morphology in a microfluidic bioreactor. (a)Metabolic activity measured by alamarBlue™ assay under static conditions and dynamic perfusion (50 µL/min). (b)Representative Live/Dead fluorescence images (10×) (calcein-AM/ethidium homodimer-1). (c – g)Quantification of total cell number (normalized to static), cell-covered area, mean cell area, equivalent diameter, and eccentricity. For image analysis, three fields per chip were averaged (n = 6 chips/condition). alamarBlue™ assay used n = 9-10 samples. Data are mean ± SD. Statistical significance was determined using unpaired two–tailed Student's t–test (c – g) or Mann–Whitney test (a) after normality assessment (*$p < 0.05$, **$p < 0.01$, ****$p < 0.0001$).

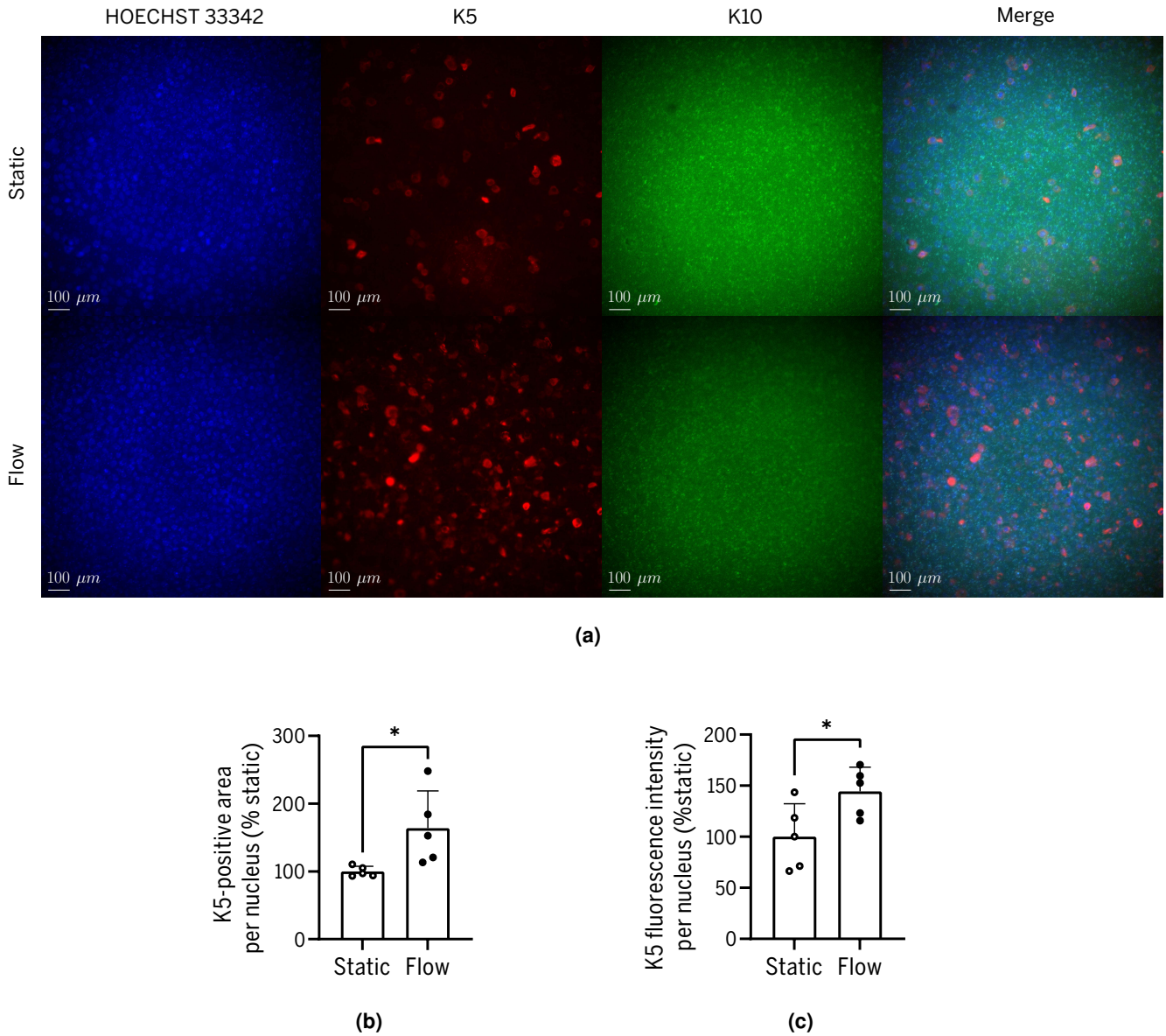


Figure 5. Flow enhances keratinocyte proliferation in proliferation medium. (a)Representative immunofluorescence images (20x) of keratinocytes under static and dynamic flow conditions. K5 (red), K10 (green), and Hoechst 33342 (blue, cell nuclei). No K10 signal was detected under proliferation conditions. (b)Quantification of K5-positive area normalized to nuclei. (c)Quantification of K5 fluorescence intensity normalized to nuclei. Each data point represents one independent chip (n = 5/condition). Data are mean ± SD. Statistical significance was determined using an unpaired two–tailed Student's t–test after normality assessment (*$p < 0.05$, **$p < 0.01$, ***$p < 0.001$).

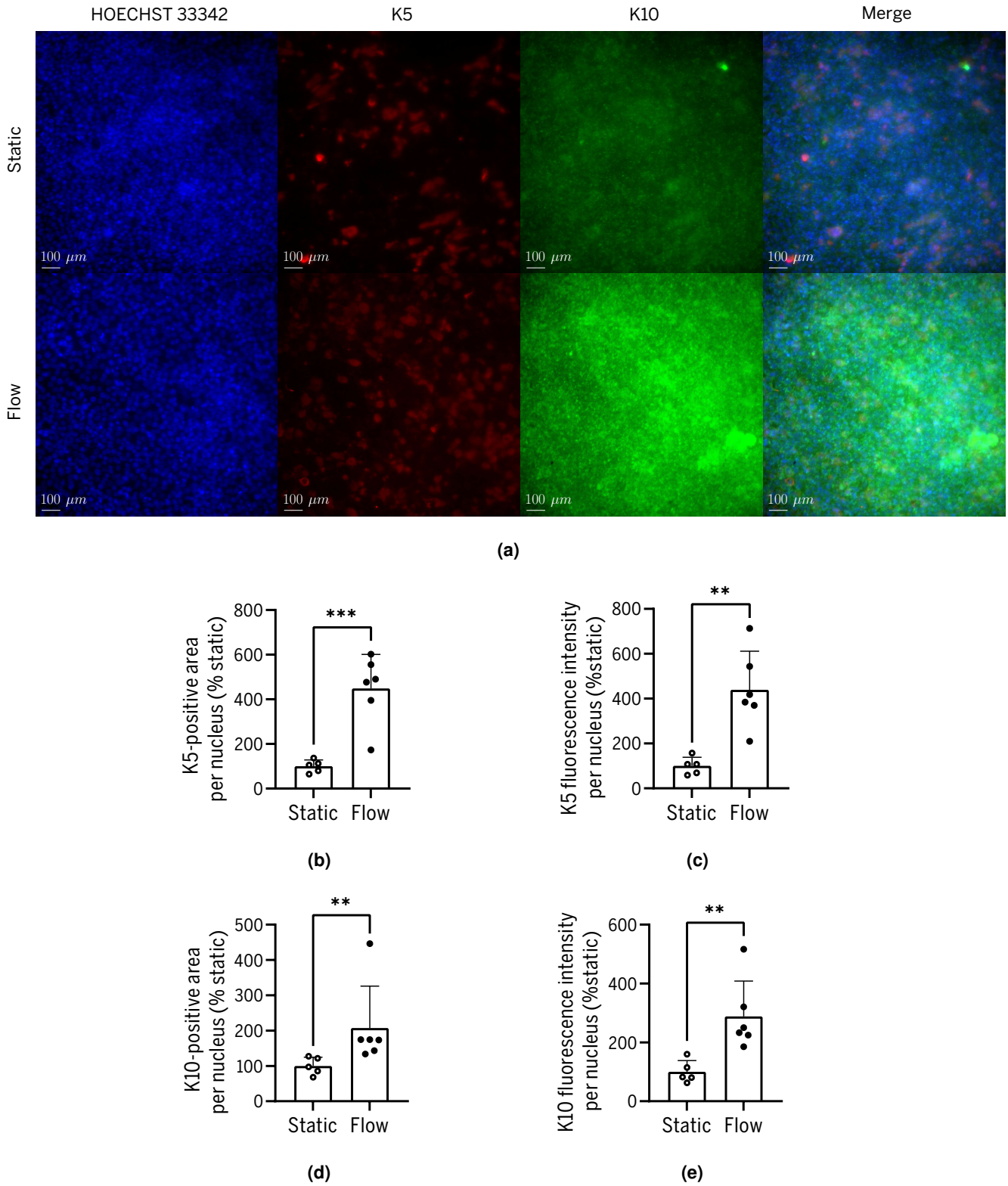


Figure 6. Dynamic perfusion promotes keratinocyte differentiation in differentiation medium. (a)Representative immunofluorescence images (20×) under static and dynamic flow conditions. K5 (red), K10 (green), nuclei (Hoechst 33342, blue). (b – e) Quantification of K5 and K10 area and fluorescence intensity normalized to nuclei and expressed relative to static (100%). Each data point represents one chip (n = 5/condition). Data are mean ± SD. Statistical significance was determined using unpaired two–tailed Student's t–test (b, c, e) or Mann–Whitney test (d) after normality testing (*$p < 0.05$, **$p < 0.01$, ***$p < 0.001$).

Discussion

This study combines a reproducible microfluidic culture platform with an optimized Human-in-the-Loop (HITL) deep learning image analysis workflow to enable quantitative evaluation of keratinocyte responses to controlled fluid flow. While the microfluidic platform provides a physiologically relevant dynamic culture environment through controlled recirculating perfusion, the computational workflow enables robust and reproducible single-cell quantification from fluorescence microscopy images. Together, these complementary experimental and computational components provide an objective framework for evaluating cellular responses under dynamic culture conditions, facilitating the development of advanced in vitro models and microphysiological systems. The combination of controlled physiological stimulation with standardized quantitative image analysis represents an important step toward improving the reproducibility and biological interpretation of microfluidic cell culture experiments.

A major contribution of this study is the implementation of a tailored HITL active learning workflow for quantitative analysis of dense epithelial cultures. Although recent trends in biomedical imaging heavily favor the deployment of massive, zero-shot foundation models (e.g., SAM architectures), our results reveal important limitations when these generalized architectures are applied to contact-inhibited tissues with diffuse boundaries. In our experiments, the Cellpose-SAM generalist model consistently under-segmented dense regions, merging neighboring cells and substantially underestimating cell number. By contrast, iterative fine-tuning of the cyto3 model through expert-guided HITL training increased single-cell detection by more than 140%, demonstrating the importance of dataset-specific optimization for quantitative image analysis.

By prioritizing a computationally lightweight architecture (cyto3) dynamically fine-tuned through expert human feedback, we successfully bypassed the severe under-segmentation artifacts endemic to generalized models. Crucially, this approach democratizes high fidelity image analysis, achieving near ground-truth precision on standard laboratory hardware. Consequently, this pipeline enabled a transition from qualitative bulk tissue approximations to robust unbiased single-cell morphometric profiling, ensuring that the subtle morphological adaptations of keratinocytes under static and flow conditions were quantified with unprecedented statistical reliability.

The benefits of the HITL workflow goes beyond improved cell counting. Automated segmentation enabled quantitative extraction of multiple single-cell descriptors, including mean live cell area and diameter, eccentricity, area normalized per nucleus and fluorescence intensity of proliferation and differentiation markers. Consequently, observations that were qualitatively apparent in microscopy images were objectively validated through quantitative analysis, reducing observer-dependent bias and improving reproducibility. This transition from qualitative assessment to robust single-cell quantification is particularly relevant for dense cultures, where manual analysis is labor-intensive and often difficult to standardize.

Despite its robust performance, several limitations of the computational workflow should be acknowledged. The primary bottleneck of the HITL approach remains its initial dependence on expert manual annotation. Although this strategy eliminates the need for large de novo training datasets, early-stage mask curation is time-consuming and requires domain-specific expertise. Furthermore, our fine-tuning model was strictly optimized for the unique topological gradients and planar geometries of 2D high-density monolayers. Extending this framework to more complex architectures, such as spheroids, 3D Organ-on-a-Chip cultures, or full-thickness skin equivalents, would require additional rounds of active learning to adapt the convolutional filters to 3D spatial relationships. Future iterations of this work will aim to expand the training pool to encompass these complex 3D morphologies, further extending the utility of accessible AI in tissue engineering.

The successful maintenance of HaCaT cells under both static and dynamic conditions confirmed the compatibility of the platform with cell culture applications. Material validation experiments demonstrated that both the individual components of the flow control system and the selected 3D-printing resin exhibited no detectable cytotoxicity, with cell viability comparable to that observed in conventional commercial culture plates. These findings are particularly relevant given the growing use of additive manufacturing in biomedical device development, where material biocompatibility remains a critical concern.

Flow culture significantly increased metabolic activity, cell number, cell-covered area, and morphometric parameters compared with static culture conditions. Together, these findings indicate that dynamic perfusion promotes keratinocyte growth while maintaining high viability and morphology. One possible explanation is that continuous recirculation improves nutrient availability and waste removal while simultaneously exposing cells to controlled mechanical stimulation. Similar observations have been reported previously, showing that fluid shear stress positively modulates keratinocyte behavior by promoting cell cycle progression and enhancing metabolic activity[27,28].

In addition to its effects on proliferation, flow was associated with increased cell area and equivalent diameter while preserving overall cell shape. The absence of significant changes in eccentricity suggests that keratinocytes expanded in size without substantial alterations in cellular morphology. This observation is consistent

with mechanotransduction-mediated responses, whereby mechanical stimuli are converted into intracellular biochemical signals that regulate cellular growth and proliferation. In keratinocytes, mechanical cues such as tension, shear stress, and substrate deformation activate signaling pathways and mechanosensitive calcium channels that contribute to tissue development and homeostasis[29,30]. More broadly, mechanotransduction via the cytoskeleton and focal adhesions couples external forces to proliferative responses across diverse cell types, suggesting that the applied flow acts as a mild mechanical stimulus, enhancing both biomass accumulation and cell division[31–33]. Consequently, the observed increase in cell size under perfusion may reflect enhanced cellular growth responses induced by continuous flow.

An additional finding of this study is the influence of dynamic culture on keratinocyte differentiation. As expected, K10 expression was not detected under proliferation conditions, consistent with maintenance of a basal proliferative phenotype. However, when cells were exposed to differentiation medium supplemented with ascorbic acid, flow conditions significantly increased both K5 and K10 expression relative to static culture. These observations are consistent with previous studies demonstrating that ascorbic acid promotes keratinocyte maturation and epidermal differentiation[34].

Importantly, all marker quantifications were normalized to the number of nuclei identified through automated analysis of Hoechst-stained images using the HITL-optimized workflow. Therefore, the increased expression of K5 and K10 cannot be explained solely by the higher cell densities observed under flow conditions. Instead, these results suggest that dynamic perfusion modulates keratinocyte phenotype in addition to promoting cell expansion. Together, the simultaneous increase in K5 and K10 expression is consistent with enhanced progression toward an early differentiated keratinocyte phenotype under differentiation conditions.

These results demonstrate that the system not only sustains cell viability but also modulates cell phenotype via environmental cues, a critical feature for developing physiologically relevant skin models. These observations agree with previous reports demonstrating that dynamic microenvironments influence keratinocyte metabolic activity, regulate cell cycle progression, guide differentiation, promote epidermal stratification, and support long-term tissue viability compared to static cultures[35,36]. The ability to simultaneously support proliferative activity and differentiation-associated responses is particularly relevant for the development of more physiologically representative in vitro skin models.

From an engineering perspective, the compact architecture of the platform enabled operation within standard incubators while supporting parallel culture of multiple independent experimental units. In addition, recirculating perfusion allows dynamic culture using relatively small medium volumes, a characteristic that may contribute to retention of cell-secreted factors within the culture system preserving autocrine and paracrine signaling[37,38]. These features provide a practical and scalable format for implementing dynamic culture conditions in routine laboratory workflows.

Several biological limitations should nevertheless be considered. The present work focused exclusively on HaCaT monocultures, whereas native skin contains multiple interacting cell populations including fibroblasts, melanocytes, immune cells, and endothelial cells. Furthermore, long-term culture stability, epithelial stratification, barrier formation, and vascular interactions were not evaluated. Future studies should investigate co-culture configurations, more complex tissue architectures, and alternative flow profiles or mechanical stimulation regimes to better understand how biomechanical signals regulate epidermal development and homeostasis.

In conclusion, this work establishes an experimental-computational workflow that combines controlled microfluidic culture with automated deep learning-based image analysis for reproducible quantitative evaluation of cellular responses under dynamic conditions. By integrating standardized flow control, validated biocompatible materials, and objective fluorescence microscopy analysis, the proposed workflow provides a scalable and reproducible strategy for quantitative evaluation of advanced in vitro and microphysiological systems. Beyond the specific application presented here, this methodology may facilitate the broader adoption of physiologically relevant dynamic culture models in biomedical research, drug discovery, toxicology, and NAMs.

Methods

Experimental and Technical Design

The microfluidic tissue culture platform consists of a flow control system, a custom-made microfluidic bioreactor, and a culture medium reservoir interconnected through PTFE tubing 1/16" OD and 1/4-28 flangeless PTFE+PFA fittings (Darwin microfluidics) (Figure S1a). The entire system was designed to operate inside a standard humidified incubator maintained at $37\ ^{\circ}\mathrm{C}$, $5\%\ \mathrm{CO_2}$, and 95% relative humidity during cell culture experiments. The main objective of this experimental setup was to generate tissue culture with a controlled automated flow inside the controlled

homogeneous environment of the incubator. The microfluidic bioreactor comprises a custom-designed culture chamber compatible with standard cell culture inserts (Falcon® Cell culture inserts, $8\ \mu\mathrm{m}$ pore size, transparent membrane for 24 well plate). The chamber is connected to the inlet and outlet microchannels, enabling the continuous flow of the culture medium beneath the insert containing the cell culture. The inlet channel is connected to the flow control system, and the outlet channel is connected to a medium reservoir, allowing recirculation and stable operation during long-term experiments with small amounts of nutrients medium.

The internal geometry of the chamber was designed to ensure a uniform flow distribution throughout the culture area while minimizing dead volumes. The dimensions of the chamber, together with the width and height of the microchannels and the internal volume of the device, were defined during the CAD design process to ensure compatibility with the selected flow range ($5 - 500\ \mu\mathrm{L/min}$) and to maintain stable flow conditions during the experiments (Figure S2).

Several components of the flow control system and microfluidic bioreactor were manufactured using stereolithography (SLA) 3D-printing. Different commercially available resins were evaluated and one was selected based on its biocompatibility and printing resolution, which are critical parameters for the manufacturing of microfluidic features.

CAD models were designed using Autodesk Inventor®, and the devices were printed using an Asiga Max X27. After printing, parts were subjected to standard post-processing procedures, including removal of the uncured resin with isopropanol and UV light exposure, according to the manufacturer recommendation.

AI-Based Image Analysis of Microscopy Data

Optical pre-processing was performed to mitigate out-of-focus inherent to imaging high-density, contact-inhibited HaCaT cells monolayers, raw Z-stacks were imported into ImageJ and subjected to a Sum Slices Z-projection. This integration method was strategically chosen over standard Maximum Intensity Projections (MIP) to maximize the signal-to-noise ratio and preserve continuous spatial gradients across cellular boundaries, ensuring no topological data was lost prior to computational analysis.

Quantitative processing of viability images and differentiation markers (K5/K10) was performed using an iterative computational workflow. Original micrographs were bicubic upsampling. Deep learning model training and quantitative morphometric analyzes were executed within a custom Python environment (Python Software Foundation v3.9.25) configured via Miniconda (Anaconda Software Distribution, 2026). The core computational pipeline relied on several specialized open-source libraries: numpy for high-performance multidimensional array manipulation, scikit-image for advanced mathematical morphology, and Cellpose (v3.0) for neural network-based single-cell segmentation. Complementary image pre-processing was performed using ImageJ. Hardware-accelerated training and inference were conducted using an NVIDIA GeForce GTX 1050 Ti GPU, demonstrating the computational accessibility and efficiency of the chosen architecture.

Spatial standardization and iterative HITL pipeline single-cell segmentation was performed utilizing the Cellpose cyto3 base architecture[19,23]. A critical step for optimal network performance involved spatial standardization using Cellpose's native upsample_cyto3 module. Because high-density HaCaT cells exhibit significantly reduced physical diameters due to contact inhibition, the raw input features risk falling below the optimal spatial frequencies expected by the cyto3 receptive field. By empirically defining the average target cell diameter and inputting this parameter into the upsampling algorithm, the images were dynamically scaled. This step ensured that the cellular topographical features precisely matched the network pre-trained convolutional filters, thereby maximizing baseline feature extraction.

To achieve near ground-truth precision on these spatially optimized images, a cumulative HITL active learning strategy was implemented. Specifically, the workflow consisted of a sequential iterative loop: an initial image was segmented using the base Cellpose cyto3 model, manually corrected by an expert, and used to fine-tune the base model. This updated model was then deployed to predict the next image, the predictions were manually refined, and the model was fine-tuned again using a cumulative training pool containing ground-truth masks from both the current and all previous iterations. This sequential accumulation of data deeply adapted the network to the complex contact topologies of the monolayer while effectively preventing catastrophic forgetting.

Post-processing and morphometric feature extraction

Quantitative Morphometric and Fluorescence Analysis

Following instance segmentation, quantitative single-cell descriptors were extracted from the generated masks using the *scikit-image* library. To ensure physical relevance, pixel-based measurements were converted to micrometers using a calibrated spatial scaling factor (C), determined by the specific objective lens and sensor physical pixel size. The physical area (A) of each cell was calculated as the total number of pixels (N) within the segmented mask

multiplied by the squared spatial calibration factor:

$$A = N \times C^2 \tag{1}$$

To standardize the representation of cell size regardless of shape irregularities, the equivalent diameter (D_{eq}) was computed. This metric represents the diameter of a perfect circle with an area identical to that of the segmented cell:

$$D_{eq} = 2\sqrt{\frac{A}{\pi}} \tag{2}$$

Cellular morphology was evaluated through eccentricity (e). This was mathematically determined by fitting an ellipse with the same second-order moments as the segmented region. Eccentricity was calculated using the lengths of the semi-major axis (a) and the semi-minor axis (b) of this fitted ellipse:

$$e = \sqrt{1 - \frac{b^2}{a^2}} \tag{3}$$

An eccentricity value of 0 represents a perfect circle (indicative of rounded morphology), while values approaching 1 represent highly elongated cells.

Finally, specific biomarker expression (e.g., K5, K10, calcein-AM, and ethidium homodimer-1) was quantified by mapping the segmented instances back to the original multichannel fluorescence images. The mean fluorescence intensity (I_{mean}) for each cell was calculated as the arithmetic mean of the intensity values (I_i) of all pixels contained within the cell's mask boundary:

$$I_{mean} = \frac{1}{N}\sum_{i=1}^{N} I_i \tag{4}$$

Population-Level Metrics and Biomarker Normalization

Beyond single-cell descriptors, macroscopic metrics were calculated to assess the overall monolayer status per field of view (FOV). The relative cell number, representing the proportion of a specific subpopulation (e.g., live cells, P_{live}) relative to the entire population, was calculated by dividing the number of live instances (N_{live}) by the total sum of live and dead cells (N_{total}):

$$P_{live}(\%) = \left(\frac{N_{live}}{N_{total}}\right) \times 100 \tag{5}$$

To quantify tissue confluency, the cell-covered area percentage (C_{area}) was extracted. This was determined by computing the ratio of the cumulative physical area of all segmented instances within the image ($\sum_{i=1}^{N_{total}} A_i$) to the total physical area of the imaging canvas (A_{FOV}):

$$C_{area}(\%) = \left(\frac{\sum_{i=1}^{N_{total}} A_i}{A_{FOV}}\right) \times 100 \tag{6}$$

Finally, the expression of epithelial differentiation markers (K5 and K10) was quantitatively normalized to the cell density to prevent density-dependent biases. The positive area per nucleus ($A_{marker/nucleus}$) was computed by dividing the total segmented fluorescent area of the specific keratin marker (A_{marker}) by the total number of detected nuclei (N_{nuclei}) within the same analyzed region:

$$A_{marker/nucleus} = \frac{A_{marker}}{N_{nuclei}} \tag{7}$$

Flow Control System and Bioreactor Operation

The flow control system is based on a piezoelectric micropump and a micro flow meter with an automated closed-loop control to ensure continuous controlled recirculating flow. The flow control system was operated remotely via Bluetooth using a custom-developed software, which allows input of the desired flow rate for the operation, ensuring stable and reproducible flow conditions during experiments.

The system was designed to operate in a recirculation mode, allowing the same culture medium to continuously circulate between the reservoir and the bioreactor. This configuration enables the use of relatively small medium volumes while maintaining long-term flow conditions. The minimum operational volume of the system depends on the internal dead volume of the bioreactor chamber ($\sim 50\ \mu\mathrm{L}$), the dead volume of the flow control system ($\sim 300\ \mu\mathrm{L}$), and the length of the connecting tubing. Under the experimental configuration used in this study, the minimum working volume was $\sim 500\ \mu\mathrm{L}$. For the experiments reported here, a $1\ \mathrm{mL}$ culture medium reservoir was used to ensure stable operation during prolonged perfusion experiments.

Material Biocompatibility Assessment

Each individual material component of the flow controller and candidate 3D-printing resins were anonymized and identified numerically throughout the study to preserve proprietary aspects of the platform design and material selection process. Materials and resins were incubated in culture medium at $37\ ^{\circ}\mathrm{C}$ for 72 hours to allow potential leachable compounds to diffuse into the medium. The conditioned medium was then applied to HaCaT cells cultured in standard 24-well plates to evaluate cytotoxicity (Figure S1b). Cell viability was measured using the alamarBlue™ assay (Invitrogen, ref. DAL1025) after 24 hours of exposure, following the manufacturer instructions. A commercial culture plate without added materials was used as a positive biocompatibility control, while a known cytotoxic material served as a negative control. Live/Dead viability assays (Invitrogen, ref. MP03224) were also performed to corroborate the alamarBlue™ results and assess cell viability and proliferative capacity of cells cultured in 3D-printed bioreactors compared with commercial culture plates, following the manufacturer instructions.

Cell Culture

Immortalized human keratinocyte HaCaT cells were obtained from Cytion (Heidelberg, Germany) and maintained in DMEM GlutaMAX™ (Gibco, ref. 10566016) supplemented with 10% fetal bovine serum (FBS; Merck, ref. F7524) and 1% penicillin–streptomycin (Gibco™, ref. 15070063). Cells were cultured under standard conditions at $37\ ^{\circ}\mathrm{C}$ in a humidified incubator with $5\%\ \mathrm{CO_2}$. Cells between passages 3 and 10 were used for all experiments. For seeding optimization experiments, cells were seeded into 24-well cell culture inserts at densities of 100000, 150000, 200000 $\mathrm{cells/cm^2}$. Cell proliferation was assessed at days 1 and 3 post-seeding using the alamarBlue™ assay. Based on these results, a seeding density of $100000\ \mathrm{cells/cm^2}$ was selected for all subsequent experiments, as it provided optimal cell growth and viability under experimental conditions.

Static and Dynamic Culture Conditions

After an initial 24 hours of the cells seeded into the inserts in standard culture plates to allow their attachment to the membrane, the inserts were transferred to custom-made microfluidic bioreactors. Cells were subsequently maintained either under static conditions (no flow) or under continuous flow using the flow control system.

For flow culture experiments, culture medium flow through the bioreactor at a constant flow rate of $50\ \mu\mathrm{L/min}$ for an additional 1 or 3 days, depending on the experimental (Figure S1c-d). Under static conditions, the inserts were kept in the same bioreactors containing the same culture medium without flow during the same time to compare it.

Cell Viability and Proliferation Assays

Cell metabolic activity was quantified using the alamarBlue™ assay (Invitrogen, ref. DAL1025) according to the manufacturer instructions. Absorbance was measured at $570\ \mathrm{nm}$ and $600\ \mathrm{nm}$ using a microplate reader (Synergy™ HTX Multi-Mode), and metabolic activity was calculated according to the standard alamarBlue™ assay reduction method.

Cell viability was further assessed using a Live/Dead viability assay (Invitrogen, ref. MP03224) based on calcein-AM and ethidium homodimer-1, which stain viable and dead cells, respectively. Fluorescence imaging was performed using a fluorescence microscope to evaluate cell viability and morphology.

Calcein-AM fluorescence was detected at approximately ex/em $495/515\ \mathrm{nm}$, while ethidium homodimer-1 fluorescence was detected at approximately ex/em $495/635\ \mathrm{nm}$.

Differentiation Medium and flow

To promote keratinocyte differentiation, the culture medium was modified by reducing the FBS concentration from 10% to 1% and supplementing the medium with $50\ \mu\mathrm{g/mL}$ ascorbic acid.

Cells were initially cultured for 24 hours in proliferation medium to allow proper adhesion to the membrane of the inserts. After this initial period, the differentiation medium was introduced into the system and flows through the bioreactor at a constant flow rate of $50\ \mu\mathrm{L/min}$ for 3 additional days (Figure S1d).

Immunofluorescence Analysis

Keratinocyte differentiation was evaluated by immunofluorescence staining of K5, a marker of basal proliferative keratinocytes, and K10, which is associated with early epidermal differentiation.

Cells were fixed with 4% paraformaldehyde, permeabilized with 0.1% Triton X-100, and blocked with 3% bovine serum albumin (BSA; Sigma-Aldrich, ref A9418) to reduce non-specific binding. Primary antibodies against K5 (Cytokeratinocin 5 Policlonal antibody; Invitrogen, ref. Pa5-32465, conc:1:400) and K10 (Cytokeratinocin 10 Monoclonal antibody; ThermoFisher Scientific, ref. MA5-13705, conc:1:400) were applied and incubated overnight at $4\ ^{\circ}\mathrm{C}$, followed by incubation with the corresponding fluorescent secondary antibodies Goat anti-Rabbit IgG (H+L) Cross-Adsorbed secondary antibody, Alexa Fluor™ 488 (Invitrogen, ref. A-11008) and Goat anti-moyse IgG (H+L) Cross-Adsorbed Secondart antibody, Alexa Fluor™ 594 (Invitrogen, ref. A11005). Cell nuclei were counterstained with Hoechst 33342 (Invitrogen, H21492; dilution 1:1000 in PBS, 5 minutes). Fluorescence images were acquired using a fluorescence microscope (Inverted Leica DMi8 microscope equipped with a Hamammatsu Orca Flash 3.0 CMOS camera) equipped with a 20× objective. Images were acquired under identical exposure settings for all experimental conditions to allow quantitative comparison. The resulting images were subsequently processed using an AI-based segmentation pipeline for quantitative single-cell analysis, enabling the extraction of fluorescence intensity and cellular morphology descriptors.

Statistical Analysis

All experiments were conducted using independent biological replicates, with sample sizes ranging from $\mathrm{n} = 3$ to $\mathrm{n} = 10$, depending on the assay. For image-based analyzes, three images per chip were acquired and averaged to obtain a single value per chip, which was considered the experimental unit. Data are presented as mean ± standard deviation (SD). Data normality was assessed prior to statistical testing. For comparisons involving more than two groups, normally distributed data were analyzed using one-way analysis of variance (ANOVA) followed by Tukey's or Dunnett's post hoc test. Non-normally distributed data were analyzed using the Kruskal–Wallis test followed by Dunn's multiple comparison test. For comparisons between two independent groups, an unpaired two-tailed Student's t-test was applied. A $\mathrm{p-value} < 0.05$ was considered statistically significant. All statistical analyzes were performed with GraphPad Prism (GraphPad Software, USA).

References

1. Franco, N. H. Animal experiments in biomedical research: a historical perspective. *Animals* **3**, 238–273, DOI: 10.3390/ani3010238 (2013).
2. Landi, M., Everitt, J. & Berridge, B. Bioethical, reproducibility, and translational challenges of animal models. *ILAR journal* **62**, 60–65, DOI: 10.1093/ilar/ilaa027 (2021).
3. Russell, W. & Burch, R. The principles of humane experimental technique. *Tech. London: Methuen* DOI: 10.5694/j.1326-5377.1960.tb73127.x (1959).
4. Sneddon, L. U., Halsey, L. G. & Bury, N. R. Considering aspects of the 3rs principles within experimental animal biology. *J. Exp. Biol.* **220**, 3007–3016, DOI: 10.1242/jeb.147058 (2017).
5. OECD. Guidance document on good in vitro method practices (givimp). https://www.oecd.org/content/dam/oecd/en/publications/reports/2018/12/guidance-document-on-good-in-vitro-method-practices-givimp_g1g938a9/9789264304796-en.pdf, DOI: 10.1787/9789264304796-en (2018). Accessed: 2026-05-08.
6. Kang, S.-M. Recent advances in microfluidic-based microphysiological systems. *BioChip J.* **16**, 13–26, DOI: 10.1007/s13206-021-00043-y (2022).
7. Kwon, D. The age of animal experiments is waning. where will science go next? *Nature* **650**, 812–814, DOI: 10.1038/d41586-026-00563-3 (2026).
8. Ortseifen, V., Viefhues, M., Wobbe, L. & Grünberger, A. Microfluidics for biotechnology: bridging gaps to foster microfluidic applications. *Front. Bioeng. Biotechnol.* **8**, 589074, DOI: 10.3389/fbioe.2020.589074 (2020).

9. Kimura, H., Sakai, Y. & Fujii, T. Organ/body-on-a-chip based on microfluidic technology for drug discovery. *Drug metabolism pharmacokinetics* **33**, 43–48, DOI: 10.1016/j.dmpk.2017.11.003 (2018).

10. Zhang, B. & Radisic, M. Organ-on-a-chip devices advance to market. *Lab on a Chip* **17**, 2395–2420, DOI: 10.1039/C6LC01554A (2017).

11. Low, L. A., Mummery, C., Berridge, B. R., Austin, C. P. & Tagle, D. A. Organs-on-chips: into the next decade. *Nat. Rev. Drug Discov.* **20**, 345–361, DOI: 10.1038/s41573-020-0079-3 (2021).

12. Zhao, Y. *et al.* Integrating organoids and organ-on-a-chip devices. *Nat. Rev. Bioeng.* **2**, 588–608, DOI: 10.1038/s44222-024-00207-z (2024).

13. Ewart, L. *et al.* Performance assessment and economic analysis of a human liver-chip for predictive toxicology. *Commun. Medicine* **2**, 154, DOI: 10.1038/s43856-022-00209-1 (2022).

14. Ismayilzada, N. *et al.* Skin-on-a-chip technologies towards clinical translation and commercialization. *Biofabrication* **16**, 042001, DOI: 10.1088/1758-5090/ad5f55 (2024).

15. Quílez, C. *et al.* Targeting the complexity of in vitro skin models: a review of cutting-edge developments. *J. Investig. Dermatol.* **144**, 2650–2670, DOI: 10.1016/j.jid.2024.04.032 (2024).

16. Kaiser, K., Bendixen, S. M., Sørensen, J. A. & Brewer, J. R. From static to dynamic: The influence of mechanotransduction on skin equivalents analyzed by bioimaging and rnaseq. *Mater. Today Bio* **25**, 101010, DOI: 10.1016/j.mtbio.2024.101010 (2024).

17. Moen, E. *et al.* Deep learning for cellular image analysis. *Nat. methods* **16**, 1233–1246, DOI: 10.1038/s41592-019-0403-1 (2019).

18. Liu, Z. *et al.* A survey on applications of deep learning in microscopy image analysis. *Comput. biology medicine* **134**, 104523, DOI: 10.1016/j.compbiomed.2021.104523 (2021).

19. Stringer, C. & Pachitariu, M. Cellpose3: one-click image restoration for improved cellular segmentation. *Nat. methods* **22**, 592–599, DOI: 10.1038/s41592-025-02595-5 (2025).

20. Archit, A. *et al.* Segment anything for microscopy. *Nat. methods* **22**, 579–591, DOI: 10.1038/s41592-024-02580-4 (2025).

21. Woodhams, B. & Uhlmann, V. From images to understanding: Advances in deep learning for cellular dynamics analysis. *Curr. Opin. Cell Biol.* **97**, 102585, DOI: 10.1016/j.ceb.2025.102585 (2025).

22. Budd, S., Robinson, E. C. & Kainz, B. A survey on active learning and human-in-the-loop deep learning for medical image analysis. *Med. image analysis* **71**, 102062, DOI: 10.1016/j.media.2021.102062 (2021).

23. Pachitariu, M. & Stringer, C. Cellpose 2.0: how to train your own model. *Nat. methods* **19**, 1634–1641, DOI: 10.1038/s41592-022-01663-4 (2022).

24. Nguyen, N. *et al.* Microfluidic models of the human circulatory system: versatile platforms for exploring mechanobiology and disease modeling. *Biophys. Rev.* **13**, 769–786, DOI: 10.1007/s12551-021-00815-8 (2021).

25. Sebastian, B. & Dittrich, P. S. Microfluidics to mimic blood flow in health and disease. *Annu. review fluid mechanics* **50**, 483–504, DOI: 10.1146/annurev-fluid-010816-060246 (2018).

26. Warner, R. L. *et al.* Full-field flicker evoked changes in parafoveal retinal blood flow. *Sci. Reports* **10**, 16051, DOI: 10.1038/s41598-020-73032-0 (2020).

27. O'Neill, A. T., Monteiro-Riviere, N. A. & Walker, G. M. Characterization of microfluidic human epidermal keratinocyte culture. *Cytotechnology* **56**, 197–207, DOI: 10.1007/s10616-008-9149-9 (2008).

28. Fernandez-Carro, E. *et al.* Modeling an optimal 3d skin-on-chip within microfluidic devices for pharmacological studies. *Pharmaceutics* **14**, 1417, DOI: 10.3390/pharmaceutics14071417 (2022).

29. Reichelt, J. Mechanotransduction of keratinocytes in culture and in the epidermis. *Eur. journal cell biology* **86**, 807–816, DOI: 10.1016/j.ejcb.2007.06.004 (2007).

30. Agarwal, T., Narayana, G. H. & Banerjee, I. Keratinocytes are mechanoresponsive to the microflow-induced shear stress. *Cytoskeleton* **76**, 209–218, DOI: 10.1002/cm.21521 (2019).

31. Vogel, V. & Sheetz, M. Local force and geometry sensing regulate cell functions. *Nat. reviews Mol. cell biology* **7**, 265–275, DOI: 10.1038/nrm1890 (2006).

32. DuFort, C. C., Paszek, M. J. & Weaver, V. M. Balancing forces: architectural control of mechanotransduction. *Nat. reviews Mol. cell biology* **12**, 308–319, DOI: 10.1038/nrm3112 (2011).

33. Espina, J. A., Cordeiro, M. H., Milivojevic, M., Pajić-Lijaković, I. & Barriga, E. H. Response of cells and tissues to shear stress. *J. Cell Sci.* **136**, jcs260985, DOI: 10.1242/jcs.260985 (2023).

34. Moll, R., Divo, M. & Langbein, L. The human keratins: biology and pathology. *Histochem. cell biology* **129**, 705–733, DOI: 10.1007/s00418-008-0435-6 (2008).

35. Sutterby, E., Thurgood, P., Baratchi, S., Khoshmanesh, K. & Pirogova, E. Microfluidic skin-on-a-chip models: Toward biomimetic artificial skin. *Small* **16**, 2002515, DOI: 10.1002/smll.202002515 (2020).

36. Jones, C. F., Di Cio, S., Connelly, J. T. & Gautrot, J. E. Design of an integrated microvascularized human skin-on-a-chip tissue equivalent model. *Front. bioengineering biotechnology* **10**, 915702, DOI: 10.3389/fbioe.2022.915702 (2022).

37. Bhatia, S. N. & Ingber, D. E. Microfluidic organs-on-chips. *Nat. biotechnology* **32**, 760–772, DOI: 10.1038/nbt.2989 (2014).

38. Sung, J. H., Koo, J. & Shuler, M. L. Mimicking the human physiology with microphysiological systems (mps). *BioChip J.* **13**, 115–126, DOI: 10.1007/s13206-019-3201-z (2019).

Author contributions statement

M. Del Valle-Fuentes: Resources, Data curation, Software, Formal Analysis, Validation, Investigation, Visualization, Methodology, Writing - original draft. **A. Corral**: Resources, Investigation. **A. Bernaldo de Quirós**: Conceptualization, Resources, Software, Supervision, Funding Acquisition, Validation, Investigation, Writing - review & editing. **O. Crespo-Toca**: Resources, Investigation. **L. Aguado-Cabanillas**: Resources, Software, Writing - review & editing. **L. Valencia**: Investigation, Writing - review & editing. **D. Velasco**: Conceptualization, Resources, Supervision, Funding Acquisition, Project administration, Writing - review & editing. **A.E. Quintero**: Conceptualization, Resources, Data Curation, Formal analysis, Supervision, Funding acquisition, Validation, Investigation, Visualization, Methodology, Writing - original draft, Project administration, Writing - review & editing. **V. Pena-Leon**: Conceptualization, Resources, Data Curation, Formal analysis, Supervision, Validation, Investigation, Visualization, Methodology, Writing - original draft, Writing - review & editing.

Additional information

Data Availability Data will be made available on request. **Competing interests** The authors declare that there is no conflict of interest regarding the publication of this article.

Funding statement

This work was supported by the MICIU/AEI /10.13039/501100011033 and NextGenerationEU/ PRTR under project CPP2021-008396-MISTICA.

Supplementary Files

This is a list of supplementary files associated with this preprint. Click to download.

- SupplementaryMaterialScientificReports.zip
- SupplementaryScientificReports.pdf
- FigureS1.pdf
- FigureS2.pdf